

Measurement of Deeply Virtual Compton Scattering and its t -dependence at HERA

H1 Collaboration

Abstract

A measurement of elastic deeply virtual Compton scattering $\gamma^*p \rightarrow \gamma p$ using e^-p collision data recorded with the H1 detector at HERA is presented. The analysed data sample corresponds to an integrated luminosity of 145 pb^{-1} . The cross section is measured as a function of the virtuality Q^2 of the exchanged photon and the centre-of-mass energy W of the γ^*p system in the kinematic domain $6.5 < Q^2 < 80 \text{ GeV}^2$, $30 < W < 140 \text{ GeV}$ and $|t| < 1 \text{ GeV}^2$, where t denotes the squared momentum transfer at the proton vertex. The cross section is determined differentially in t for different Q^2 and W values and exponential t -slope parameters are derived. The measurements are compared to a NLO QCD calculation based on generalised parton distributions. In the context of the dipole approach, the geometric scaling property of the DVCS cross section is studied for different values of t .

Submitted to Phys. Lett. **B**

F.D. Aaron^{5,49}, A. Aktas¹¹, C. Alexa⁵, V. Andreev²⁵, B. Antunovic¹¹, S. Aplin¹¹, A. Asmone³³,
 A. Astvatsatourov⁴, S. Backovic³⁰, A. Baghdasaryan³⁸, P. Baranov^{25,†}, E. Barrelet²⁹,
 W. Bartel¹¹, S. Baudrand²⁷, M. Beckingham¹¹, K. Begzsuren³⁵, O. Behnke¹⁴, O. Behrendt⁸,
 A. Belousov²⁵, N. Berger⁴⁰, J.C. Bizot²⁷, M.-O. Boenig⁸, V. Boudry²⁸, I. Bozovic-Jelisavcic²,
 J. Bracinik²⁶, G. Brandt¹⁴, M. Brinkmann¹¹, V. Brisson²⁷, D. Bruncko¹⁶, F.W. Büsser¹²,
 A. Bunyatyan^{13,38}, G. Buschhorn²⁶, L. Bystritskaya²⁴, A.J. Campbell¹¹, K.B. Cantun Avila²²,
 F. Cassol-Brunner²¹, K. Cerny³², V. Cerny^{16,47}, V. Chekelian²⁶, A. Cholewa¹¹,
 J.G. Contreras²², J.A. Coughlan⁶, G. Cozzika¹⁰, J. Cvach³¹, J.B. Dainton¹⁸, K. Daum^{37,43},
 M. Deak¹¹, Y. de Boer²⁴, B. Delcourt²⁷, M. Del Degan⁴⁰, J. Delvax⁴, A. De Roeck^{11,45},
 E.A. De Wolf⁴, C. Diaconu²¹, V. Dodonov¹³, A. Dossanov²⁶, A. Dubak^{30,46}, G. Eckerlin¹¹,
 V. Efremenko²⁴, S. Egli³⁶, R. Eichler³⁶, F. Eisele¹⁴, A. Eliseev²⁵, E. Elsen¹¹, S. Essenov²⁴,
 A. Falkiewicz⁷, P.J.W. Faulkner³, L. Favart⁴, A. Fedotov²⁴, R. Felst¹¹, J. Feltesse^{10,48},
 J. Ferencei¹⁶, L. Finke¹¹, M. Fleischer¹¹, A. Fomenko²⁵, G. Franke¹¹, T. Frisson²⁸,
 E. Gabathuler¹⁸, J. Gayler¹¹, S. Ghazaryan³⁸, A. Glazov¹¹, I. Glushkov³⁹, L. Goerlich⁷,
 M. Goettlich¹², N. Gogitidze²⁵, S. Gorbounov³⁹, M. Gouzevitch²⁸, C. Grab⁴⁰, T. Greenshaw¹⁸,
 B.R. Grell¹¹, G. Grindhammer²⁶, S. Habib^{12,50}, D. Haidt¹¹, M. Hansson²⁰, G. Heinzelmann¹²,
 C. Helebrant¹¹, R.C.W. Henderson¹⁷, H. Henschel³⁹, G. Herrera²³, M. Hildebrandt³⁶,
 K.H. Hiller³⁹, D. Hoffmann²¹, R. Horisberger³⁶, A. Hovhannisyan³⁸, T. Hreus^{4,44},
 M. Jacquet²⁷, M.E. Janssen¹¹, X. Janssen⁴, V. Jemanov¹², L. Jönsson²⁰, D.P. Johnson^{4,†},
 A.W. Jung¹⁵, H. Jung¹¹, M. Kapichine⁹, J. Katzy¹¹, I.R. Kenyon³, C. Kiesling²⁶, M. Klein¹⁸,
 C. Kleinwort¹¹, T. Klimkovich¹¹, T. Kluge¹¹, A. Knutsson¹¹, R. Kogler²⁶, V. Korbel¹¹,
 P. Kostka³⁹, M. Kraemer¹¹, K. Krastev¹¹, J. Kretzschmar³⁹, A. Kropivnitskaya²⁴, K. Krüger¹⁵,
 K. Kutak¹¹, M.P.J. Landon¹⁹, W. Lange³⁹, G. Laštovička-Medin³⁰, P. Laycock¹⁸,
 A. Lebedev²⁵, G. Leibenguth⁴⁰, V. Lendermann¹⁵, S. Levonian¹¹, G. Li²⁷, L. Lindfeld⁴¹,
 K. Lipka¹², A. Liptaj²⁶, B. List¹², J. List¹¹, N. Loktionova²⁵, R. Lopez-Fernandez²³,
 V. Lubimov²⁴, A.-I. Lucaci-Timoce¹¹, L. Lytkin¹³, A. Makankine⁹, E. Malinovski²⁵,
 P. Marage⁴, Ll. Marti¹¹, H.-U. Martyn¹, S.J. Maxfield¹⁸, A. Mehta¹⁸, K. Meier¹⁵,
 A.B. Meyer¹¹, H. Meyer¹¹, H. Meyer³⁷, J. Meyer¹¹, V. Michels¹¹, S. Mikocki⁷,
 I. Milcewicz-Mika⁷, A. Mohamed¹⁸, F. Moreau²⁸, A. Morozov⁹, J.V. Morris⁶, M.U. Mozer⁴,
 M. Mudrinic², K. Müller⁴¹, P. Murín^{16,44}, K. Nankov³⁴, B. Naroska¹², Th. Naumann³⁹,
 P.R. Newman³, C. Niebuhr¹¹, A. Nikiforov¹¹, G. Nowak⁷, K. Nowak⁴¹, M. Nozicka³⁹,
 B. Olivier²⁶, J.E. Olsson¹¹, S. Osman²⁰, D. Ozerov²⁴, V. Palichik⁹, I. Panagoulas^{1,11,42},
 M. Pandurovic², Th. Papadopoulou^{1,11,42}, C. Pascaud²⁷, G.D. Patel¹⁸, H. Peng¹¹, E. Perez¹⁰,
 D. Perez-Astudillo²², A. Perieanu¹¹, A. Petrukhin²⁴, I. Picuric³⁰, S. Piec³⁹, D. Pitzl¹¹,
 R. Plačakytė¹¹, R. Polifka³², B. Povh¹³, T. Preda⁵, P. Prideaux¹⁸, V. Radescu¹¹, A.J. Rahmat¹⁸,
 N. Raicevic³⁰, A. Raspiareza²⁶, T. Ravdandorj³⁵, P. Reimer³¹, C. Risler¹¹, E. Rizvi¹⁹,
 P. Robmann⁴¹, B. Roland⁴, R. Roosen⁴, A. Rostovtsev²⁴, Z. Rurikova¹¹, S. Rusakov²⁵,
 D. Salek³², F. Salvaire¹¹, D.P.C. Sankey⁶, M. Sauter⁴⁰, E. Sauvan²¹, S. Schmidt¹¹,
 S. Schmitt¹¹, C. Schmitz⁴¹, L. Schoeffel¹⁰, A. Schöning⁴⁰, H.-C. Schultz-Coulon¹⁵,
 F. Sefkow¹¹, R.N. Shaw-West³, I. Sheviakov²⁵, L.N. Shtarkov²⁵, T. Sloan¹⁷, I. Smiljanic²,
 P. Smirnov²⁵, Y. Soloviev²⁵, D. South⁸, V. Spaskov⁹, A. Specka²⁸, Z. Staykova¹¹, M. Steder¹¹,
 B. Stella³³, J. Stiewe¹⁵, U. Straumann⁴¹, D. Sunar⁴, T. Sykora⁴, V. Tchoulakov⁹,
 G. Thompson¹⁹, P.D. Thompson³, T. Toll¹¹, F. Tomasz¹⁶, T.H. Tran²⁷, D. Traynor¹⁹,
 T.N. Trinh²¹, P. Truöl⁴¹, I. Tsakov³⁴, B. Tseepeldorj³⁵, I. Tsurin³⁹, J. Turnau⁷,
 E. Tzamariudaki²⁶, K. Urban¹⁵, A. Valkárová³², C. Vallée²¹, P. Van Mechelen⁴, A. Vargas
 Trevino¹¹, Y. Vazdik²⁵, S. Vinokurova¹¹, V. Volchinski³⁸, G. Weber¹², R. Weber⁴⁰,

D. Wegener⁸, C. Werner¹⁴, M. Wessels¹¹, Ch. Wissing¹¹, R. Wolf¹⁴, E. Wunsch¹¹,
V. Yeganov³⁸, J. Žáček³², J. Zálešák³¹, Z. Zhang²⁷, A. Zhelezov²⁴, A. Zhokin²⁴, Y.C. Zhu¹¹,
T. Zimmermann⁴⁰, H. Zohrabyan³⁸, and F. Zomer²⁷

- ¹ *I. Physikalisches Institut der RWTH, Aachen, Germany^a*
² *Vinca Institute of Nuclear Sciences, Belgrade, Serbia*
³ *School of Physics and Astronomy, University of Birmingham, Birmingham, UK^b*
⁴ *Inter-University Institute for High Energies ULB-VUB, Brussels; Universiteit Antwerpen, Antwerpen; Belgium^c*
⁵ *National Institute for Physics and Nuclear Engineering (NIPNE), Bucharest, Romania*
⁶ *Rutherford Appleton Laboratory, Chilton, Didcot, UK^b*
⁷ *Institute for Nuclear Physics, Cracow, Poland^d*
⁸ *Institut für Physik, Universität Dortmund, Dortmund, Germany^a*
⁹ *Joint Institute for Nuclear Research, Dubna, Russia*
¹⁰ *CEA, DSM/DAPNIA, CE-Saclay, Gif-sur-Yvette, France*
¹¹ *DESY, Hamburg, Germany*
¹² *Institut für Experimentalphysik, Universität Hamburg, Hamburg, Germany^a*
¹³ *Max-Planck-Institut für Kernphysik, Heidelberg, Germany*
¹⁴ *Physikalisches Institut, Universität Heidelberg, Heidelberg, Germany^a*
¹⁵ *Kirchhoff-Institut für Physik, Universität Heidelberg, Heidelberg, Germany^a*
¹⁶ *Institute of Experimental Physics, Slovak Academy of Sciences, Košice, Slovak Republic^f*
¹⁷ *Department of Physics, University of Lancaster, Lancaster, UK^b*
¹⁸ *Department of Physics, University of Liverpool, Liverpool, UK^b*
¹⁹ *Queen Mary and Westfield College, London, UK^b*
²⁰ *Physics Department, University of Lund, Lund, Sweden^g*
²¹ *CPPM, CNRS/IN2P3 - Univ. Mediterranee, Marseille - France*
²² *Departamento de Física Aplicada, CINVESTAV, Mérida, Yucatán, México^j*
²³ *Departamento de Física, CINVESTAV, México^j*
²⁴ *Institute for Theoretical and Experimental Physics, Moscow, Russia*
²⁵ *Lebedev Physical Institute, Moscow, Russia^e*
²⁶ *Max-Planck-Institut für Physik, München, Germany*
²⁷ *LAL, Univ Paris-Sud, CNRS/IN2P3, Orsay, France*
²⁸ *LLR, Ecole Polytechnique, IN2P3-CNRS, Palaiseau, France*
²⁹ *LPNHE, Universités Paris VI and VII, IN2P3-CNRS, Paris, France*
³⁰ *Faculty of Science, University of Montenegro, Podgorica, Montenegro^e*
³¹ *Institute of Physics, Academy of Sciences of the Czech Republic, Praha, Czech Republic^h*
³² *Faculty of Mathematics and Physics, Charles University, Praha, Czech Republic^h*
³³ *Dipartimento di Fisica Università di Roma Tre and INFN Roma 3, Roma, Italy*
³⁴ *Institute for Nuclear Research and Nuclear Energy, Sofia, Bulgaria^e*
³⁵ *Institute of Physics and Technology of the Mongolian Academy of Sciences, Ulaanbaatar, Mongolia*
³⁶ *Paul Scherrer Institut, Villigen, Switzerland*
³⁷ *Fachbereich C, Universität Wuppertal, Wuppertal, Germany*
³⁸ *Yerevan Physics Institute, Yerevan, Armenia*
³⁹ *DESY, Zeuthen, Germany*
⁴⁰ *Institut für Teilchenphysik, ETH, Zürich, Switzerlandⁱ*

⁴¹ *Physik-Institut der Universität Zürich, Zürich, Switzerlandⁱ*

⁴² *Also at Physics Department, National Technical University, Zografou Campus, GR-15773 Athens, Greece*

⁴³ *Also at Rechenzentrum, Universität Wuppertal, Wuppertal, Germany*

⁴⁴ *Also at University of P.J. Šafárik, Košice, Slovak Republic*

⁴⁵ *Also at CERN, Geneva, Switzerland*

⁴⁶ *Also at Max-Planck-Institut für Physik, München, Germany*

⁴⁷ *Also at Comenius University, Bratislava, Slovak Republic*

⁴⁸ *Also at DESY and University Hamburg, Helmholtz Humboldt Research Award*

⁴⁹ *Also at Faculty of Physics, University of Bucharest, Bucharest, Romania*

⁵⁰ *Supported by a scholarship of the World Laboratory Björn Wiik Research Project*

† *Deceased*

^a *Supported by the Bundesministerium für Bildung und Forschung, FRG, under contract numbers 05 H1 1GUA /1, 05 H1 1PAA /1, 05 H1 1PAB /9, 05 H1 1PEA /6, 05 H1 1VHA /7 and 05 H1 1VHB /5*

^b *Supported by the UK Particle Physics and Astronomy Research Council, and formerly by the UK Science and Engineering Research Council*

^c *Supported by FNRS-FWO-Vlaanderen, IISN-IKW and IWT and by Interuniversity Attraction Poles Programme, Belgian Science Policy*

^d *Partially Supported by Polish Ministry of Science and Higher Education, grant PBS/DESY/70/2006*

^e *Supported by the Deutsche Forschungsgemeinschaft*

^f *Supported by VEGA SR grant no. 2/7062/ 27*

^g *Supported by the Swedish Natural Science Research Council*

^h *Supported by the Ministry of Education of the Czech Republic under the projects LC527 and INGO-1P05LA259*

ⁱ *Supported by the Swiss National Science Foundation*

^j *Supported by CONACYT, México, grant 48778-F*

^l *This project is co-funded by the European Social Fund (75%) and National Resources (25%) - (EPEAEK II) - PYTHAGORAS II*

1 Introduction

Measurements of inclusive deep-inelastic scattering (DIS) of leptons and nucleons allow the extraction of Parton Distribution Functions (PDFs) which describe the fraction of the longitudinal momentum of the nucleon carried by the quarks, anti-quarks and gluons. A shortfall of this approach is that the PDFs contain information neither on the correlations between partons nor on their transverse distributions. This missing information can be provided by measurements of processes in which the nucleon remains intact and the four momentum transfer squared at the nucleon vertex, t , is non-zero [1–6]. The simplest such reaction is deeply virtual Compton scattering (DVCS), the diffractive scattering of a virtual photon off a proton $\gamma^*p \rightarrow \gamma p$. In high energy electron-proton collisions at HERA, DVCS is accessed through the reaction $ep \rightarrow e\gamma p$ [7–9]. This reaction also receives a contribution from the purely electromagnetic Bethe-Heitler (BH) process, where the photon is emitted from the electron. The BH cross section is precisely calculable in QED and can be subtracted from the total process rate to extract the DVCS cross section.

Perturbative QCD calculations assume that the DVCS reaction involves two partons in the proton which carry different longitudinal and transverse momenta. The difference in longitudinal momentum of the two involved partons, also called skewing, is a consequence of the mass difference between the incoming virtual photon and the outgoing real photon. The skewing can be described by introducing generalised parton distributions (GPDs) [1–5], which are functions of the two unequal momenta and thus encode information on the longitudinal momentum correlations of partons. Information on the transverse momentum of partons is incorporated in the t -dependence of GPDs [2–5]. The t -dependent functions follow particular equations for their evolution as a function of the four momentum transfer squared Q^2 of the exchanged virtual photon [3–5]. These evolution equations still need to be tested.

The DVCS cross section can also be interpreted within the dipole model [10–12]. In this picture the virtual photon fluctuates into a colour singlet $q\bar{q}$ pair (or dipole) of a transverse size $r \sim 1/Q$, which subsequently undergoes hard scattering with the gluons in the proton [13]. At very small values of the Bjorken scaling variable x the saturation regime of QCD can be reached. In this domain, the gluon density in the proton is so large that non-linear effects like gluon recombination tame its growth. In the dipole model approach, the transition to the saturation regime is characterised by the so-called saturation scale parametrised here as $Q_s(x) = Q_0(x_0/x)^{-\lambda/2}$, where Q_0 , x_0 and λ are parameters [14]. The transition to saturation occurs when Q becomes comparable to $Q_s(x)$. An important feature of dipole models that incorporate saturation is that the total cross section can be expressed as a function of the single variable τ :

$$\sigma_{tot}^{\gamma^*p}(x, Q^2) = \sigma_{tot}^{\gamma^*p}(\tau), \quad \text{with} \quad \tau = \frac{Q^2}{Q_s^2(x)}. \quad (1)$$

This property, called geometric scaling, has already been observed to hold for the total ep DIS cross section [15, 16] as well as in DIS on nuclear targets [17] and in diffractive processes [12]. It has also recently been addressed in the context of exclusive processes including DVCS [12] and extended to cases with non-zero momentum transfer to the proton [18].

This paper presents a new measurement of single and double differential DVCS cross sections as a function of Q^2 and the γ^*p centre-of-mass energy W . The single differential cross

section $d\sigma/dt$ is also extracted. The data were recorded in the years 2005 and 2006 with the H1 detector when HERA collided protons of 920 GeV energy with 27.6 GeV electrons. The sample corresponds to an integrated luminosity of 145 pb^{-1} , four times larger than the previous H1 measurement [8] of DVCS in positron-proton collisions. The measurement is carried out in the kinematic range $6.5 < Q^2 < 80 \text{ GeV}^2$, $30 < W < 140 \text{ GeV}$ and $|t| < 1 \text{ GeV}^2$. The t -dependence of the DVCS cross section, $d\sigma/dt$, is found to be well approximated by an exponential form $e^{-b|t|}$; this parametrisation is used throughout the paper. The Q^2 and W dependences of b are studied. A parametrisation of the observed Q^2 dependence of b is used to constrain the normalisation of the pQCD predictions based on GPDs. The validity of the skewed evolution equations is tested. The geometric scaling property of DVCS is also investigated and the cross section is compared with dipole model predictions. The scaling property is studied for the first time for different values of t .

2 Experimental Conditions and Monte Carlo Simulation

A detailed description of the H1 detector can be found in [19]. Here, only the detector components relevant for the present analysis are described. H1 uses a right-handed coordinate system with the z axis along the beam direction, the $+z$ or “forward” direction being that of the outgoing proton beam. The polar angle θ is defined with respect to the z axis and the pseudo-rapidity is given by $\eta = -\ln \tan \theta/2$. The SpaCal [20], a lead scintillating fibre calorimeter, covers the backward region ($153^\circ < \theta < 176^\circ$). Its energy resolution for electromagnetic showers is $\sigma(E)/E \simeq 7.1\%/\sqrt{E/\text{GeV}} \oplus 1\%$. The liquid argon (LAr) calorimeter ($4^\circ \leq \theta \leq 154^\circ$) is situated inside a solenoidal magnet. The energy resolution for electromagnetic showers is $\sigma(E)/E \simeq 11\%/\sqrt{E/\text{GeV}}$ as obtained from test beam measurements [21]. The main component of the central tracking detector is the central jet chamber CJC ($20^\circ < \theta < 160^\circ$) which consists of two coaxial cylindrical drift chambers with wires parallel to the beam direction. The measurement of charged particle transverse momenta is performed in a magnetic field of 1.16 T, which is uniform over the full tracker volume. The innermost proportional chamber CIP ($9^\circ < \theta < 171^\circ$) is used in this analysis to complement the CJC in the backward region for the reconstruction of the interaction vertex. The forward muon detector (FMD) consists of a series of drift chambers covering the range $1.9 < \eta < 3.7$. Primary particles produced at larger η can be detected indirectly in the FMD if they undergo a secondary scattering with the beam pipe or other adjacent material. Therefore, the FMD is used in this analysis to provide an additional veto against inelastic or proton dissociative events. The luminosity is determined from the rate of Bethe-Heitler processes measured using a calorimeter located close to the beam pipe at $z = -103 \text{ m}$ in the backward direction.

A dedicated event trigger was set up for this analysis. It is based on topological and neural network algorithms and uses correlations between electromagnetic energy deposits of electrons or photons in both the LAr and the SpaCal [26]. The combined trigger efficiency is close to 100%.

Monte Carlo (MC) simulations are used to estimate the background contributions and the corrections that must be applied to the data to account for the finite acceptance and the resolution of the detectors. Elastic DVCS events in ep collisions are generated using the Monte Carlo

generator MILOU [22], based on the cross section calculation from [23] and using a t -slope parameter $b = 5.45 \text{ GeV}^{-2}$, as determined in this analysis (see section 5.1). Inelastic DVCS events in which the proton dissociates into a baryonic system Y are also simulated with MILOU setting the t -slope b_{pdiss} to 1.2 GeV^{-2} , as determined in a dedicated study (see section 3). The Monte Carlo program COMPTON 2.0 [24] is used to simulate elastic and inelastic BH events. The background source of diffractive meson events is simulated using the DIFFVM Monte Carlo [25]. All generated events are passed through a detailed simulation of the H1 detector and are subject to the same reconstruction and analysis chain as the data.

3 Event Selection

In elastic DVCS events, the scattered electron and the photon are the only particles that should give signals in the detector [8]. The scattered proton escapes undetected through the beam pipe. The selection of the analysis event sample requires the scattered electron to be detected in the SpaCal and the photon in the LAr. The energy of the scattered electron candidate must be greater than 15 GeV. The photon is required to have a transverse momentum P_T above 2 GeV and a polar angle between 25° and 145° . Events are selected if there are either no tracks at all or a single central track which is associated with the scattered electron. In order to reject inelastic and proton dissociation events, no further energy deposit in the LAr calorimeter larger than 1 GeV is allowed and no activity above the noise level should be present in the FMD. The influence of QED radiative corrections is reduced by the requirement that the longitudinal momentum balance $E - P_z$ be greater than 45 GeV. Here, E denotes the energy and P_z the momentum along the beam axis of all measured final state particles. To enhance the DVCS signal with respect to the BH contribution and to ensure a large acceptance, the kinematic domain is restricted to $6.5 < Q^2 < 80 \text{ GeV}^2$ and $30 < W < 140 \text{ GeV}$.

The selected analysis sample contains 2538 events. It is dominated by elastic DVCS events, but also contains contributions from the elastic BH process and from the BH and DVCS processes with proton dissociation, $e^-p \rightarrow e^- \gamma Y$, where the baryonic system Y of mass M_Y is undetected. These background contributions are studied in further detail. A control sample of BH events is selected. For this sample, it is required that the electron be detected in the LAr and the photon in the SpaCal (see [8] for more details). The COMPTON MC describes accurately the normalisation and the shapes of the distributions of the kinematic variables for these events. The deviations are within 3%, and this value is used subsequently as an estimate for the systematic uncertainty on this contribution. A second control sample dominated by inelastic BH and DVCS processes is obtained by selecting events with a signal in the FMD. After subtracting the inelastic BH contribution, as estimated from the COMPTON MC, this sample allows the normalisation of the inelastic DVCS process to be determined. Within the model used in MILOU [22], the normalisation of the inelastic contribution is directly related to the exponential t -slope parameter. The measured event yield corresponds to an exponential t distribution with a slope of 1.2 GeV^{-2} which is subsequently used in the simulation of inelastic DVCS events. The corresponding contribution of proton dissociation in the analysis event sample is found to be $16 \pm 5\%$. Other backgrounds from diffractive ω and ϕ production with decay modes to final states including photons are estimated to be negligible in the kinematic range of the analysis.

Contamination from processes with low multiplicity π^0 production was also investigated and found to be negligible.

The reconstruction method for the kinematic variables Q^2 , x and W relies on the measured polar angles of the final state electron and photon (double angle method) [8]. The variable t is approximated by the negative square of the transverse momentum of the outgoing proton. The latter is computed from the vector sum of the transverse momenta of the final state photon $\vec{P}_{T\gamma}$ and of the scattered electron \vec{P}_{Te} : $t \simeq -|\vec{P}_{T\gamma} + \vec{P}_{Te}|^2$. The resolution of the t reconstruction lies in the range 0.08 to 0.22 GeV².

Distributions of selected kinematic variables are presented in figure 1 for the analysis sample. The MC expectations of the different processes are also displayed. Each source is normalised to the data luminosity. A good description of the shape and normalisation of the measured distributions is observed.

4 Cross Section Determination and Systematic Uncertainties

The DVCS and BH contributions dominate in the analysis phase space. In addition, an interference term contributes to the cross section due to the identical final states of both processes. In the leading twist approximation, the main contribution resulting from the interference of the BH and DVCS processes is proportional to the cosine of the azimuthal angle of the photon¹ [1, 27]. Since the present measurement is integrated over this angle, the contribution of the interference term is estimated to be small (below 1%). The DVCS cross section, $\gamma^*p \rightarrow \gamma p$, is evaluated in each bin i with the bin centre values Q_i^2 , W_i , t_i , from the total number N_i^{obs} of data events in the analysis sample using the expression

$$\sigma_{DVCS}(Q_i^2, W_i, t_i) = \frac{(N_i^{\text{obs}} - N_i^{\text{BH}} - N_i^{\text{p-diss}})}{N_i^{\text{DVCS}}} \cdot \sigma_{DVCS}^{\text{th}}(Q_i^2, W_i, t_i). \quad (2)$$

The other numbers in this equation are calculated using the MC simulations described in section 2. N_i^{BH} denotes the number of BH events (elastic and inelastic) reconstructed in bin i , $N_i^{\text{p-diss}}$ the number of inelastic DVCS background events, N_i^{DVCS} the number of DVCS events computed from the elastic DVCS MC and $\sigma_{DVCS}^{\text{th}}$ is the theoretical DVCS cross section used for the generation of DVCS MC events. The measured cross section is thus directly corrected for detector inefficiencies and acceptances and is expressed at each bin centre value.

The mean value of the acceptance, defined as the number of MC events reconstructed in a bin divided by the number of events generated in the same bin, is 45% over the whole kinematic range and reaches 78% for the highest t bin. The systematic errors of the measured DVCS cross section are determined by repeating the analysis after applying to the MC appropriate variations for each systematic source. The main contribution comes from the acceptance correction factors calculated by varying the t -slope parameter set in the elastic DVCS MC by $\pm 8\%$. The uncertainty on the number of elastic DVCS events lost by the application of the FMD veto is

¹The azimuthal angle of the photon is defined in the proton rest frame as the angle between the plane formed by the incoming and scattered electron and that formed by the virtual photon and the scattered proton.

modelled by a 4% variation of the FMD efficiency. Both error sources together result in an error of 10% on the measured elastic DVCS cross section. The uncertainty related to the inelastic DVCS background is estimated from the variation of its t -slope parameter by 25% around the nominal value of $b = 1.2 \text{ GeV}^{-2}$. The resulting error on the cross section amounts to 5% on average and reaches 15% at high t . The uncertainties related to trigger efficiency, photon identification efficiency, radiative corrections and the subtraction of BH background and luminosity measurement are each in the range of 2 to 4%. The total systematic uncertainty of the cross section amounts to about 15% and is dominated by correlated errors.

5 Results and Interpretations

5.1 Cross Sections and t -dependence

The complete DVCS sample is used to extract the W dependence of the DVCS cross section expressed at $Q^2 = 8 \text{ GeV}^2$ as well as the Q^2 dependence at $W = 82 \text{ GeV}$. The results are displayed in figure 2 and are in agreement within errors with the previous measurements [8, 9]. The steep rise of the cross section with W is an indication of the presence of a hard underlying process [28]. The corresponding cross section measurements are shown in table 1.

Next, the W dependence of the DVCS cross section is determined for three separate ranges of Q^2 and shown in figure 3(a). The corresponding cross section measurements are given in table 2. A fit of the form W^δ is performed to the cross section in each Q^2 range. Figure 3(b) presents the δ values obtained as a function of Q^2 . It is observed that δ is independent of Q^2 within the errors. Using the complete analysis sample, the value of δ expressed at $Q^2 = 8 \text{ GeV}^2$ is found to be $0.74 \pm 0.11 \pm 0.16$, where the first error is statistical and the second systematic.

The differential cross section as a function of t is displayed in figures 4(a) and (b) for three values of Q^2 and W , respectively. Fits of the form $d\sigma/dt \sim e^{-b|t|}$ are performed taking into account the statistical and correlated systematic errors; they describe the data well. The derived t -slope parameters $b(Q^2)$ and $b(W)$ are displayed in figures 4(c) and (d), respectively. The cross section values and the results for b in each Q^2 and W bin are given in table 3. This analysis extends the study of the evolution of b with Q^2 to larger values than in the previous H1 measurement [8]. This Q^2 dependence can be parametrised [30] as

$$b(Q^2) = A (1 - B \log(Q^2/(2 \text{ GeV}^2))). \quad (3)$$

Fitting this function to the measured b values of the present data and to the value obtained at $Q^2 = 4 \text{ GeV}^2$ in the previous H1 publication [8] yields $A = 6.98 \pm 0.54 \text{ GeV}^2$ and $B = 0.12 \pm 0.03$. The systematic errors and their point to point correlations were taken into account in the fit, resulting in a correlation coefficient between A and B of $\rho_{AB} = 0.92$. As shown in figure 4(c) the fit function provides a good description of the measured b values over the whole Q^2 range. The values of b as a function of W are measured for the first time and shown in figure 4(d). No significant variation of b with W is observed.

Using the complete analysis sample, the value of b expressed at $Q^2 = 8 \text{ GeV}^2$ is found to be $5.45 \pm 0.19 \pm 0.34 \text{ GeV}^{-2}$, where the first error is statistical and the second systematic. Following [2, 6], this t -slope value can be converted to an average impact parameter of

$\sqrt{\langle r_T^2 \rangle} = 0.65 \pm 0.02$ fm. It corresponds to the transverse extension of partons, dominated by sea quarks and gluons for an average value $x = 1.2 \cdot 10^{-3}$, in the plane perpendicular to the direction of motion of the proton. This value is related to the size of the core of the proton with no account of the peripheral soft structure.

5.2 QCD Interpretation in Terms of GPDs

The determination of $b(Q^2)$ described above can be used to study the Q^2 evolution of the GPDs. The DVCS cross section integrated over the momentum transfer t can be written [23] as

$$\sigma_{DVCS}(Q^2, W) \equiv \frac{[\mathcal{I}m A(\gamma^* p \rightarrow \gamma p)_{t=0}(Q^2, W)]^2 (1 + \rho^2)}{16\pi b(Q^2, W)}, \quad (4)$$

where $\mathcal{I}m A(\gamma^* p \rightarrow \gamma p)_{t=0}(Q^2, W)$ is the imaginary part of the $\gamma^* p \rightarrow \gamma p$ scattering amplitude at $t = 0$ and ρ^2 is a small correction due to the real part of the amplitude. In the following, ρ is determined from dispersion relations [11] to be $\rho = \tan(\frac{\pi}{2}\omega(Q^2))$. The coefficient $\omega(Q^2)$ describes the power governing the W dependence of DVCS at a given Q^2 . It is taken from the corresponding power of the rapid rise of the proton structure function F_2 at low x ($F_2 \sim x^{-\omega}$) [31], assuming that it is sufficiently close to the one in DVCS. In the GPD formalism, the amplitude $A(\gamma^* p \rightarrow \gamma p)_{t=0}$ is directly proportional to the GPDs. As shown in the previous section, the Q^2 dependence of the t -slope b is non-negligible. Therefore, the Q^2 evolution of the GPDs themselves is accessed by removing this variation of $b(Q^2)$. For this purpose, the dimensionless observable S is defined as

$$S = \sqrt{\frac{\sigma_{DVCS} Q^4 b(Q^2)}{(1 + \rho^2)}}. \quad (5)$$

Using the parametrisation (3) for $b(Q^2)$, S is then calculated for each Q^2 bin from the cross section measurements of this analysis (table 1) and from those of the previous H1 publication [8]. The uncertainties on the parameters A and B of (3) are directly propagated to determine the error on $b(Q^2)$ at any given Q^2 value. The results for S are presented in figure 5(a) together with the prediction of a GPD model [30], based on the PDFs parametrisation given in [32]. It is observed that the pQCD skewed evolution equations [3–5] provide a reasonable description of the measured weak rise of S with Q^2 .

The magnitude of the skewing effects present in the DVCS process can be extracted by constructing the ratio of the imaginary parts of the DVCS and DIS amplitudes. At leading order in α_s , this ratio $R \equiv \mathcal{I}m A(\gamma^* p \rightarrow \gamma p)_{t=0} / \mathcal{I}m A(\gamma^* p \rightarrow \gamma^* p)_{t=0}$ is equal to the ratio of the GPDs to the PDFs. The virtual photon is assumed to be mainly transversely polarised in the case of the DVCS process due to the real photon in the final state and therefore has to be taken as transversely polarised in the DIS amplitude too. The expression for R as a function of the measured observables can be written as

$$R = \frac{4 \sqrt{\pi \sigma_{DVCS} b(Q^2)}}{\sigma_T(\gamma^* p \rightarrow X) \sqrt{(1 + \rho^2)}} = \frac{\sqrt{\sigma_{DVCS} Q^4 b(Q^2)}}{\sqrt{\pi^3 \alpha_{EM} F_T(x, Q^2) \sqrt{(1 + \rho^2)}}}, \quad (6)$$

using the relation $\sigma_T(\gamma^* p \rightarrow X) = 4\pi^2\alpha_{EM}F_T(x, Q^2)/Q^2$ with $\alpha_{EM} = 1/137$. R is evaluated taking $F_T = F_2 - F_L$ from the QCD analysis presented in [33] and using the parametrisation (3) for $b(Q^2)$. The measured values of the ratio R for each Q^2 bin are shown in figure 5(b) and compared with the calculation based on the GPD model proposed in [30]. The typical values of R are around 2, whereas in a model without skewing R would be equal to unity. Therefore, the present measurement confirms the large effect of skewing. In GPD models, two different effects contribute to skewing [3–5]: the kinematics of the DVCS process and the Q^2 evolution of the GPDs. The data are compared to a model which takes only the former effect into account. The result of this incomplete model is represented by a dotted line in figure 5(b). The present measurements show that such an approximation is not sufficient to reproduce the total skewing effects observed in the data.

5.3 Geometric Scaling

As discussed in section 1, the dipole model represents another possible theoretical approach to describe the DVCS reaction. It is therefore interesting to test if the present DVCS measurements obey the geometric scaling laws predicted by such models.

In the following study parameters of the dipole model are taken from an analysis of the total DIS cross section [14, 18]. The saturation scale $Q_s(x) = Q_0(x_0/x)^{-\lambda/2}$ is evaluated using $Q_0 = 1$ GeV, $\lambda = 0.25$ and $x_0 = 2.7 \cdot 10^{-5}$. The DVCS cross section measurements listed in table 2 and those from the previous H1 publication [8] which are measured at different Q^2 and $x = Q^2/W^2$ values can be represented as a function of the single variable τ (see equation (1)). The result is shown in figure 6(a). All of the cross section measurements appear to be well aligned on a single curve as a function of τ . Therefore the DVCS data are compatible with the geometric scaling law. The dipole model of [12, 14] is also represented in figure 6(a) and gives a good description of the cross section measurements over the complete range of τ .

The dependence of the DVCS cross section on τ is also studied at four different values of t . For this purpose, the cross section is measured differentially in t for three values of W and two ranges of Q^2 ($6.5 < Q^2 < 11$ GeV² and $11 < Q^2 < 80$ GeV²), as listed in table 4. Keeping the same parameters Q_0 , λ and x_0 as previously defined, each value of the differential cross section is again represented as a function of τ . The results are shown in figure 6(b), together with the predictions of the dipole model [12, 14]. For these predictions, the t -dependence is factorised out as $e^{-b|t|}$, where the global t -slope parameter b measured in section 5.1 is used. A reasonable description of the DVCS cross section values in the four t bins is observed, with the same saturation scale $Q_s(x)$ used in all cases.

6 Conclusion

The cross section for deeply virtual Compton scattering $\gamma^*p \rightarrow \gamma p$ has been measured with the H1 detector at HERA. The analysis uses the e^-p data recorded in 2005 and 2006 corresponding to a luminosity of 145 pb^{-1} , four times larger than in the previous H1 publication [8]. The

measurement is performed in the kinematic range $6.5 < Q^2 < 80 \text{ GeV}^2$, $30 < W < 140 \text{ GeV}$ and $|t| < 1 \text{ GeV}^2$.

The W dependence of the cross section is well described by a function W^δ . No significant variation of the exponent δ as a function of Q^2 is observed. For the total sample a value $\delta = 0.74 \pm 0.11 \pm 0.16$ is determined. The steep rise of the cross section with W indicates a hard underlying process. The t -dependence of the cross section is well described by the form $e^{-b|t|}$ with an average slope of $b = 5.45 \pm 0.19 \pm 0.34 \text{ GeV}^{-2}$. This value corresponds to a transverse extension of sea quarks and gluons in the proton of $\sqrt{\langle r_T^2 \rangle} = 0.65 \pm 0.02 \text{ fm}$. The t -slopes are determined for the first time differentially in W with no significant dependence observed. The study of the Q^2 dependence of b is extended to significantly larger Q^2 values compared to previous measurements. The slopes found in the present analysis and in the previous H1 publication are in agreement with a slow decrease of b as a function of Q^2 .

The measurement of $b(Q^2)$ obtained in the present analysis is used to constrain the normalisation and Q^2 dependence of theoretical predictions based on GPDs. It is found that a GPD model reproduces well both the DVCS amplitude and its weak rise with Q^2 . The skewing effects have been investigated and are found to be large, as expected in GPD models. Another approach based on a dipole model including saturation effects predicts that the cross section can be approximated by a function of the single variable, $\tau = Q^2/Q_s^2(x)$ where $Q_s(x)$ is the saturation scale. The present measurement of the DVCS cross section is found to be compatible with such a geometric scaling using the same parameters as derived from inclusive DIS. For the first time, this scaling property is observed for different values of t .

Acknowledgements

We are grateful to the HERA machine group whose outstanding efforts have made this experiment possible. We thank the engineers and technicians for their work in constructing and maintaining the H1 detector, our funding agencies for financial support, the DESY technical staff for continual assistance and the DESY directorate for the hospitality which they extend to the non DESY members of the collaboration. We would like to thank Markus Diehl for helpful discussions.

References

- [1] M. Diehl, T. Gousset, B. Pire and J. P. Ralston, Phys. Lett. B **411** (1997) 193 [hep-ph/9706344].
- [2] M. Burkardt, Int. J. Mod. Phys. A **18** (2003) 173 [hep-ph/0207047].
- [3] M. Diehl, Eur. Phys. J. C **25** (2002) 223 [Erratum-ibid. C **31** (2003) 277] [hep-ph/0205208].
- [4] K. Kumerički, D. Müller and K. Passek-Kumerički, hep-ph/0703179.

- [5] V. Guzey and T. Teckentrup, Phys. Rev. D **74** (2006) 054027 [hep-ph/0607099].
- [6] L. Frankfurt, M. Strikman and C. Weiss, Ann. Rev. Nucl. Part. Sci. **55** (2005) 403 [hep-ph/0507286].
- [7] C. Adloff *et al.* [H1 Collaboration], Phys. Lett. B **517** (2001) 47 [hep-ex/0107005].
- [8] A. Aktas *et al.* [H1 Collaboration], Eur. Phys. J. C **44** (2005) 1 [hep-ex/0505061].
- [9] S. Chekanov *et al.* [ZEUS Collaboration], Phys. Lett. B **573** (2003) 46 [hep-ex/0305028].
- [10] A. Donnachie and H. G. Dosch, Phys. Lett. B **502** (2001) 74 [hep-ph/0010227].
- [11] L. Favart and M. V. T. Machado, Eur. Phys. J. C **29** (2003) 365 [hep-ph/0302079].
- [12] C. Marquet and L. Schoeffel, Phys. Lett. B **639** (2006) 471 [hep-ph/0606079].
- [13] A. H. Mueller, Nucl. Phys. B **335** (1990) 115;
N. N. Nikolaev and B. G. Zakharov, Z. Phys. C **49** (1991) 607.
- [14] E. Iancu, K. Itakura and S. Munier, Phys. Lett. B **590** (2004) 199 [hep-ph/0310338].
- [15] K. Golec-Biernat and M. Wüsthoff, Phys. Rev. D **59** (1999) 014017 [hep-ph/9807513].
- [16] A. M. Staśto, K. Golec-Biernat and J. Kwieciński, Phys. Rev. Lett. **86** (2001) 596 [hep-ph/0007192].
- [17] A. Freund, K. Rummukainen, H. Weigert and A. Schäfer, Phys. Rev. Lett. **90** (2003) 222002 [hep-ph/0210139].
- [18] C. Marquet, R. Peschanski and G. Soyez, hep-ph/0702171.
- [19] I. Abt *et al.* [H1 Collaboration], Nucl. Instrum. Meth. A **386** (1997) 310;
I. Abt *et al.* [H1 Collaboration], Nucl. Instrum. Meth. A **386** (1997) 348.
- [20] R. D. Appuhn *et al.* [H1 SPACAL Group], Nucl. Instrum. Meth. A **386** (1997) 397.
- [21] B. Andrieu *et al.* [H1 Calorimeter Group], Nucl. Instrum. Meth. A **350** (1994) 57.
- [22] E. Perez, L. Schoeffel and L. Favart, hep-ph/0411389.
- [23] L. L. Frankfurt, A. Freund and M. Strikman, Phys. Rev. D **58** (1998) 114001 [Erratum-
ibid. D **59** (1999) 119901] [hep-ph/9710356].
- [24] A. Courau, S. Kermiche, T. Carli and P. Kessler, *Quasi-Real QED Compton Monte Carlo, Proceedings of the Workshop on Physics at HERA*, Vol. 2: 902-915, Hamburg 1991.
- [25] B. List, A. Mastroberardino, *DIFFVM: A Monte Carlo generator for diffractive processes in ep scattering, Proceedings of the Monte Carlo Generators for HERA physics*, DESY-PROC-1999-02, p. 396.

- [26] B. Roland, “Mesure de la Diffusion Compton à Haute Virtualité à HERA II”, Ph.D. thesis, Université libre de Bruxelles (2007) (in preparation, to appear at <http://www-h1.desy.de/psfiles/theses/>).
- [27] A. V. Belitsky, D. Müller and A. Kirchner, Nucl. Phys. B **629** (2002) 323 [hep-ph/0112108].
- [28] I. P. Ivanov, N. N. Nikolaev and A. A. Savin, Phys. Part. Nucl. **37** (2006) 1 [hep-ph/0501034].
- [29] W. M. Yao *et al.* [Particle Data Group], J. Phys. G **33** (2006) 1.
- [30] A. Freund, Phys. Rev. D **68** (2003) 096006 [hep-ph/0306012].
- [31] C. Adloff *et al.* [H1 Collaboration], Phys. Lett. B **520** (2001) 183 [hep-ex/0108035].
- [32] J. Pumplin, D. R. Stump, J. Huston, H. L. Lai, P. Nadolsky and W. K. Tung, JHEP **0207** (2002) 012 [hep-ph/0201195].
- [33] C. Adloff *et al.* [H1 Collaboration], Eur. Phys. J. C **21** (2001) 33 [hep-ex/0012053].

Q^2 [GeV ²]	σ_{DVCS} [nb]	W [GeV]	σ_{DVCS} [nb]
8.75	3.59 ± 0.21 ± 0.41	45	2.91 ± 0.20 ± 0.25
15.5	1.38 ± 0.10 ± 0.21	70	3.96 ± 0.32 ± 0.37
25	0.58 ± 0.09 ± 0.09	90	4.78 ± 0.41 ± 0.57
55	0.13 ± 0.03 ± 0.04	110	5.55 ± 0.57 ± 0.88
		130	6.56 ± 1.17 ± 1.77

Table 1: The DVCS cross section $\gamma^*p \rightarrow \gamma p$, σ_{DVCS} , as a function of Q^2 for $W = 82$ GeV and as a function of W for $Q^2 = 8$ GeV², both for $|t| < 1$ GeV². The first errors are statistical, the second systematic.

W [GeV]	σ_{DVCS} [nb]		
	$Q^2 = 8$ GeV ²	$Q^2 = 15.5$ GeV ²	$Q^2 = 25$ GeV ²
45	2.60 ± 0.24 ± 0.24	0.94 ± 0.10 ± 0.10	0.35 ± 0.13 ± 0.07
70	3.15 ± 0.40 ± 0.33	1.54 ± 0.17 ± 0.14	0.36 ± 0.10 ± 0.05
90	5.25 ± 0.55 ± 0.55	0.95 ± 0.20 ± 0.17	0.83 ± 0.18 ± 0.09
110	5.11 ± 0.71 ± 0.76	1.69 ± 0.31 ± 0.33	0.90 ± 0.23 ± 0.18
130	5.88 ± 1.89 ± 1.26	2.06 ± 0.51 ± 0.56	0.90 ± 0.36 ± 0.32

Table 2: The DVCS cross section $\gamma^*p \rightarrow \gamma p$, σ_{DVCS} , as a function of W for three Q^2 values. The first errors are statistical, the second systematic.

$d\sigma_{DVCS}/dt$ [nb/GeV ²]			
$W = 82$ GeV			
$ t $ [GeV ²]	$Q^2 = 8$ GeV ²	$Q^2 = 15.5$ GeV ²	$Q^2 = 25$ GeV ²
0.10	13.1 ± 1.10 ± 1.85	4.37 ± 0.47 ± 0.86	1.41 ± 0.40 ± 0.43
0.30	4.69 ± 0.45 ± 0.55	1.02 ± 0.16 ± 0.18	0.71 ± 0.16 ± 0.08
0.50	1.37 ± 0.21 ± 0.23	0.49 ± 0.08 ± 0.08	0.28 ± 0.07 ± 0.04
0.80	0.19 ± 0.04 ± 0.06	0.12 ± 0.02 ± 0.02	0.04 ± 0.01 ± 0.02
b [GeV ⁻²]	5.84 ± 0.30 ± 0.35	5.16 ± 0.26 ± 0.30	5.09 ± 0.55 ± 0.60
$Q^2 = 10$ GeV ²			
$ t $ [GeV ²]	$W = 40$ GeV	$W = 70$ GeV	$W = 100$ GeV
0.10	4.99 ± 0.66 ± 0.54	7.78 ± 0.69 ± 0.87	10.9 ± 1.14 ± 2.36
0.30	1.45 ± 0.29 ± 0.18	2.74 ± 0.31 ± 0.30	3.47 ± 0.42 ± 0.53
0.50	0.49 ± 0.14 ± 0.08	0.81 ± 0.14 ± 0.11	1.49 ± 0.21 ± 0.24
0.80	0.12 ± 0.03 ± 0.03	0.19 ± 0.03 ± 0.03	0.19 ± 0.04 ± 0.06
b [GeV ⁻²]	5.40 ± 0.40 ± 0.25	5.34 ± 0.25 ± 0.27	5.48 ± 0.31 ± 0.45

Table 3: The DVCS cross section $\gamma^*p \rightarrow \gamma p$, differential in t , $d\sigma_{DVCS}/dt$, for three values of Q^2 at $W = 82$ GeV, and for three values of W at $Q^2 = 10$ GeV². Results for the corresponding t -slope parameters b are given. The first errors are statistical, the second systematic.

$d\sigma_{DVCS}/dt$ [nb/GeV ²]			
$Q^2 = 8$ GeV ²			
$ t $ [GeV ²]	$W = 40$ GeV	$W = 70$ GeV	$W = 100$ GeV
0.10	8.10 ± 1.22 ± 0.82	10.0 ± 1.30 ± 1.27	16.0 ± 2.11 ± 2.74
0.30	2.30 ± 0.54 ± 0.28	4.35 ± 0.63 ± 0.46	5.45 ± 0.80 ± 0.73
0.50	0.45 ± 0.22 ± 0.10	1.08 ± 0.27 ± 0.17	1.96 ± 0.41 ± 0.35
0.80	0.16 ± 0.06 ± 0.03	0.13 ± 0.06 ± 0.04	0.21 ± 0.09 ± 0.08
$Q^2 = 20$ GeV ²			
$ t $ [GeV ²]	$W = 40$ GeV	$W = 70$ GeV	$W = 100$ GeV
0.10	1.06 ± 0.28 ± 0.28	2.38 ± 0.29 ± 0.26	2.98 ± 0.49 ± 0.85
0.30	0.33 ± 0.07 ± 0.07	0.67 ± 0.12 ± 0.07	0.89 ± 0.17 ± 0.17
0.50	0.22 ± 0.06 ± 0.06	0.24 ± 0.05 ± 0.03	0.44 ± 0.08 ± 0.08
0.80	0.04 ± 0.01 ± 0.01	0.07 ± 0.01 ± 0.02	0.06 ± 0.02 ± 0.02

Table 4: The DVCS cross section $\gamma^*p \rightarrow \gamma p$, differential in t , $d\sigma_{DVCS}/dt$, for three values of W extracted in two Q^2 intervals: $6.5 < Q^2 < 11$ GeV² and $11 < Q^2 < 80$ GeV², corrected to the central values of $Q^2 = 8$ GeV² and 20 GeV², respectively. The first errors are statistical, the second systematic.

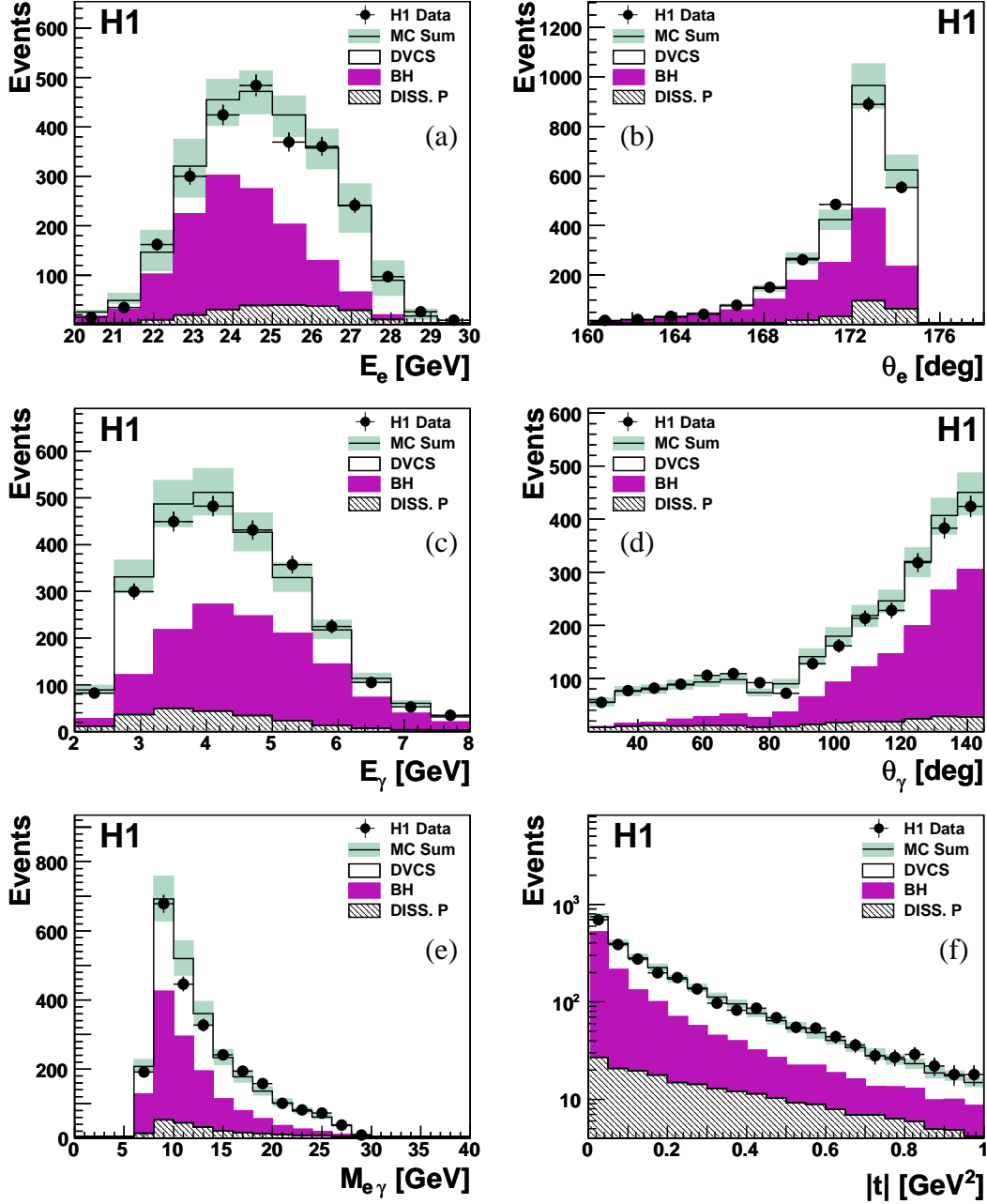


Figure 1: Distributions of the energy (a) and polar angle (b) of the scattered electron, the energy (c) and polar angle (d) of the photon, the electron-photon invariant mass (e) and the proton four momentum transfer squared $|t|$ (f). The data are compared with Monte Carlo expectations for elastic DVCS, elastic and inelastic BH and inelastic DVCS (labelled DISS. p). All Monte Carlo simulations are normalised according to the luminosity of the data. The open histogram shows the total prediction and the shaded band its estimated uncertainty.

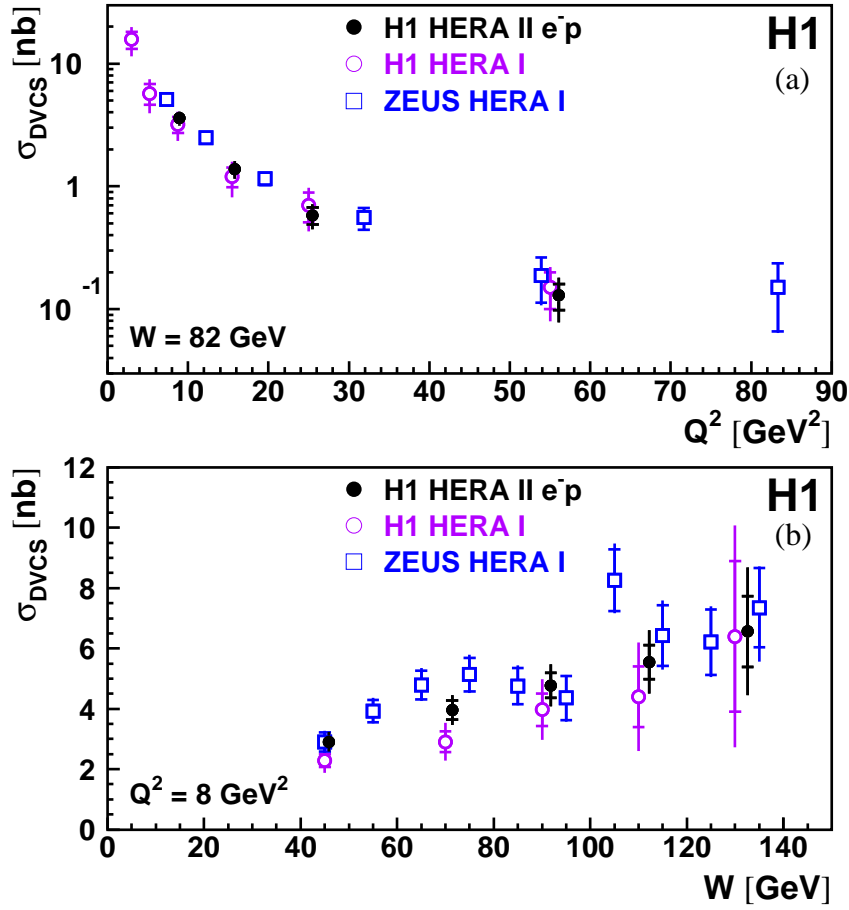


Figure 2: The DVCS cross section as a function of Q^2 at $W = 82$ GeV (a) and as a function of W at $Q^2 = 8$ GeV² (b). The results from the previous H1 and ZEUS publications [8,9] based on HERA I data are also displayed. The inner error bars represent the statistical errors, the outer error bars the statistical and systematic errors added in quadrature.

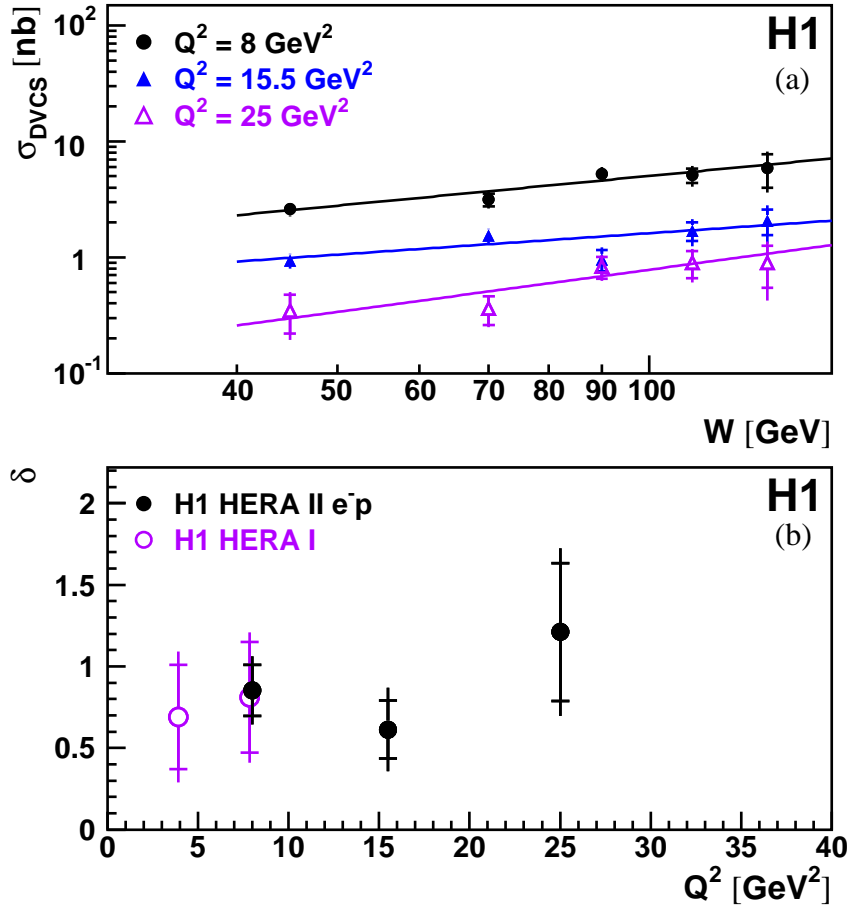


Figure 3: The DVCS cross section as a function of W at three values of Q^2 (a). The solid lines represent the results of fits of the form W^δ . The fitted values of $\delta(Q^2)$ are shown in (b). The inner error bars represent the statistical errors, the outer error bars the statistical and systematic errors added in quadrature.

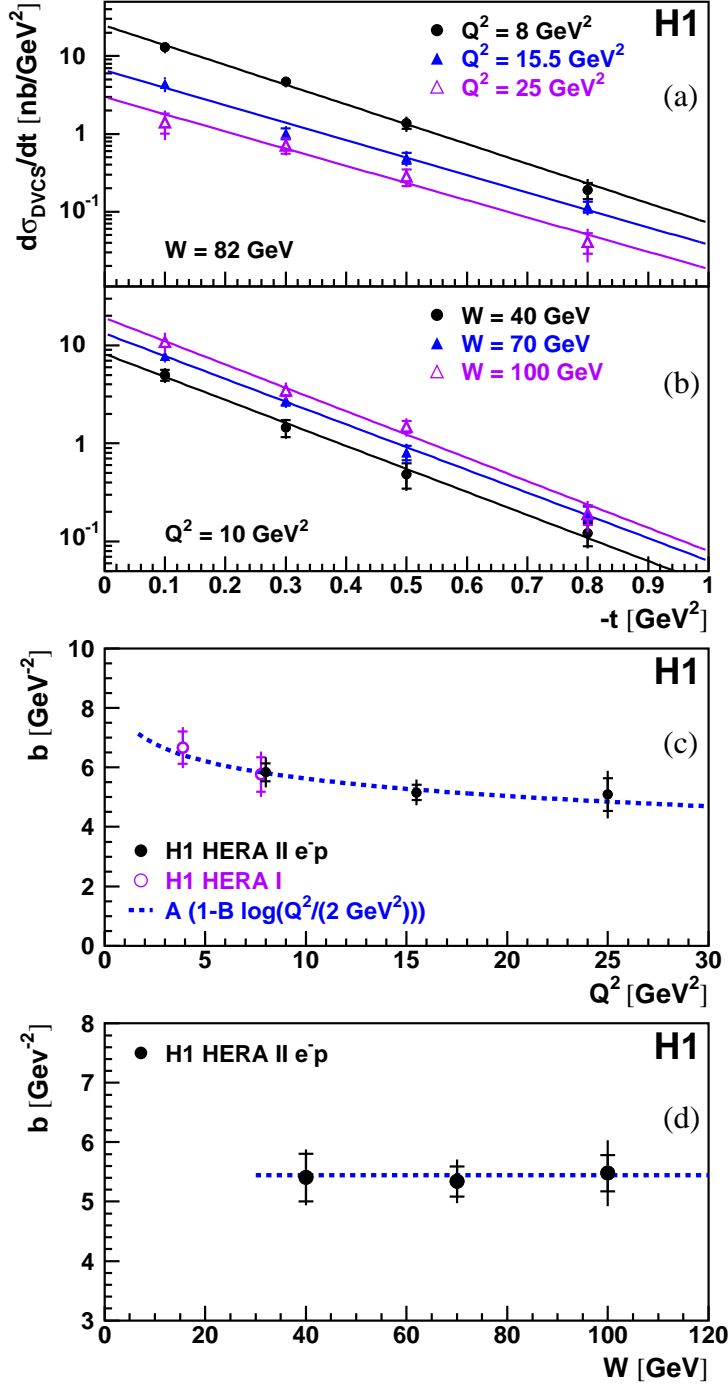


Figure 4: The DVCS cross section, differential in t , for three values of Q^2 expressed at $W = 82$ GeV (a) and for three values of W at $Q^2 = 10$ GeV 2 (b). The solid lines in (a) and (b) represent the results of fits of the form $e^{-b|t|}$. The fitted t -slope parameters $b(Q^2)$ are shown in (c) together with the t -slope parameters from the previous H1 publication [8]. The dashed curve in (c) represents the result of a fit to the $b(Q^2)$ values using a phenomenological function as described in the text. In (d) the fitted t -slope parameters $b(W)$ are shown. The dashed line in (d) corresponds to the average value $b = 5.45$ GeV 2 , obtained from a fit to the complete data sample of the present measurement. The inner error bars represent the statistical errors and the outer error bars the statistical and systematic errors added in quadrature.

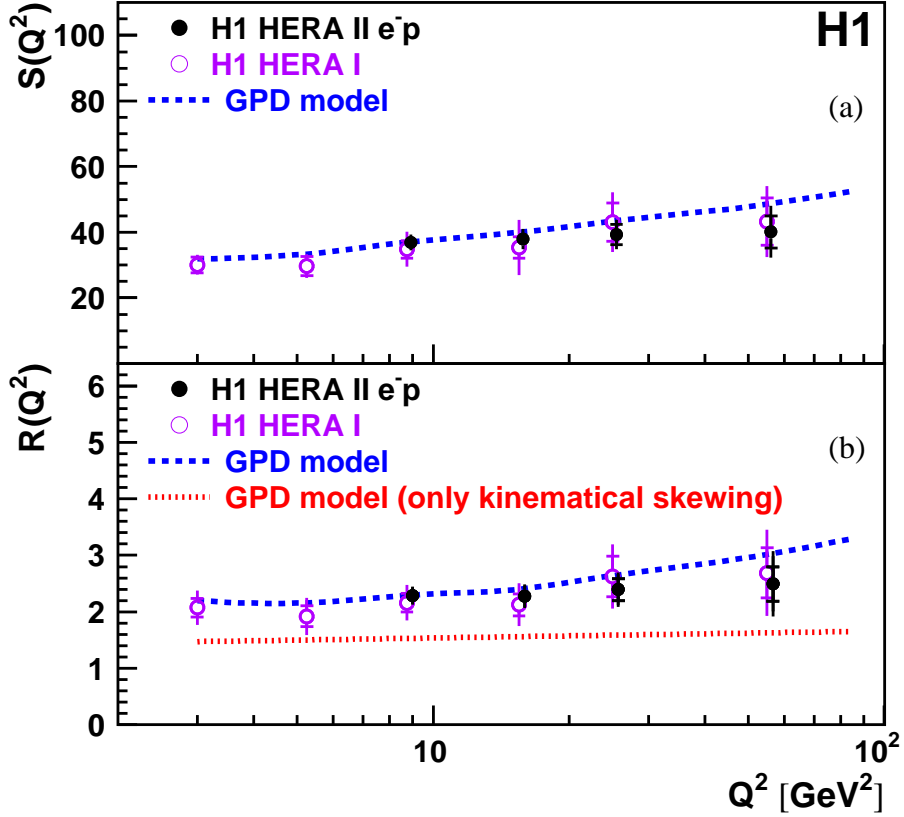


Figure 5: The observables S and R (see text), shown as a function of Q^2 in (a) and (b), respectively. The results from the previous H1 publication [8] based on HERA I data are also displayed. The inner error bars represent the statistical errors, the outer error bars the statistical and systematic errors added in quadrature. The dashed curves show the predictions of the GPD model [30, 32]. In (b), the dotted curve shows the prediction of a GPD model based on an approximation where only the kinematical part of the skewing effects are taken into account (see text).

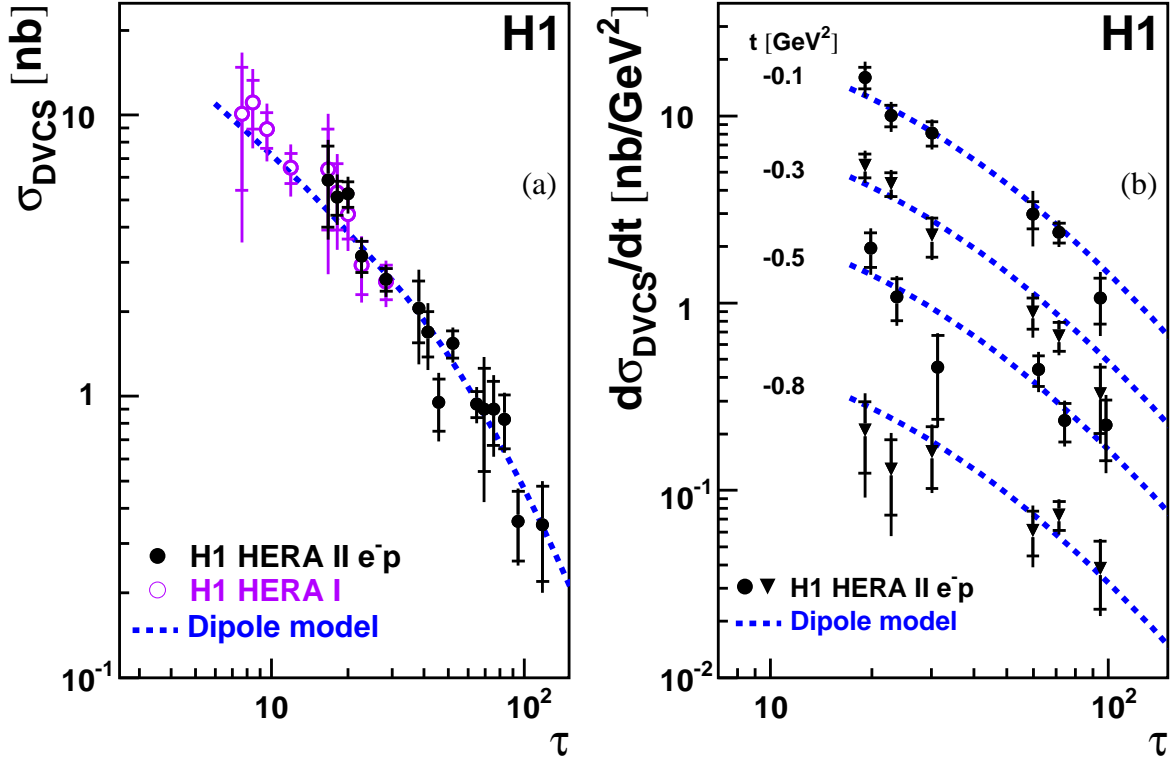


Figure 6: DVCS cross section measurements as a function of the scaling variable $\tau = Q^2/Q_s^2(x)$. In (a) the results are shown for the full t range $|t| < 1$ GeV 2 and in (b) at four values of t . The cross section measurements from the previous H1 publication [8] are also shown in (a). The inner error bars indicate the statistical errors, the outer error bars the statistical and systematic errors added in quadrature. The dashed curves represent the predictions of the dipole model [12, 14].